

Microstructure and Mechanical Behavior of ODS Stainless Steel Fabricated Using Cryomilling



CHEN DAI, LILIA KURMANAEVA, CHRIS SCHADE, ENRIQUE LAVERNIA,
and DIRAN APELIAN

Oxide-dispersion-strengthened (ODS) stainless steels have been developed as structural materials for applications at elevated temperatures. In this study, water-atomized 316L stainless steel powder was cryomilled with various types of nanosized-oxide reinforcements. Conventional sintering and field-assisted sintering techniques (FAST) were used to consolidate the cryomilled powder. Mechanical properties, both in tension and compression, were evaluated for consolidated samples: samples made of cryomilled powders, as well as samples made of a mixture of cryomilled and coarse-grained atomized powders. The bimodal structure that evolved from such mixtures effectively toughened the ultrastrong cryomilled material. Microstructural analysis was carried out to determine the efficacy of the cryomilled powder. Results from the cryomilling experiments showed that a minimum grain size could be reached within 12 hours of milling. Our results showed that dispersion of the oxide phases during cryomilling occurred exclusively through physical mechanisms, which was different from that previously reported for room-temperature ball milling. The spatial distribution of the oxide dispersoids was found to be dependent on the evolution of internal surfaces during milling and on the type of oxide particle used. Finally, the influence of reinforcement on the mechanical behavior of the cryomilled material was analyzed using oxide-dispersion-strengthening and load-transfer-based strengthening mechanisms.

<https://doi.org/10.1007/s11661-019-05479-4>

© The Minerals, Metals & Materials Society and ASM International 2019

I. INTRODUCTION

THE demand to limit global exhaust gas emissions and fuel consumption has prompted the need to build smaller engines with optimal engine power output for transportation purposes.^[1] A turbocharger is an effective approach to decrease the size of high-output engines. However, in order to achieve better combustion efficiency, the temperature of the exhaust gas from a turbocharger engine must be significantly raised compared to that of conventional piston engines; and this requires the timely development of compatible materials for turbochargers that operate efficiently at temperatures as high as 1323 K (1050 °C). A candidate material

currently being explored for this particular application is oxide-dispersion-strengthened (ODS) steel, which can be much more cost effective than the Inconel family of alloys that have been commonly used.^[2] ODS steels contain submicron or nanoscale oxides which are dispersed evenly throughout the steel matrix to pin on dislocations and grain boundaries in order to retain the strength at elevated temperatures.^[3] In this manner, ODS steels are also suitable for other extremely severe environmental applications, such as those in the nuclear and aerospace industries.^[4]

A commercially viable method to fabricate ODS steels involves mechanical milling, followed by pressing and sintering. Compared to fabrication methods involving precipitation reactions^[5] or oxidation reactions on either the surface^[6] or in the interior,^[7] mechanical alloying is considered to be a versatile technique for producing ODS steels because of the simplicity of the process, the associated economic benefits, and its ability to generate nonequilibrium phases (such as oxides) in the system.^[8] In this study, cryogenic ball milling (cryomilling) is used to blend oxide particles into a stainless steel matrix. Cryomilling is essentially mechanical attrition under a liquid cryogenic environment. By utilizing cryomilling, it is expected that oxides will be effectively dispersed, while recovery and recrystallization are suppressed by the

CHEN DAI and LILIA KURMANAEVA are with the Department of Chemical Engineering and Material Science, University of California, Davis, Davis, CA 95616. CHRIS SCHADE is with the Hoeganaes Corporation, Cinnaminson, NJ 08077. ENRIQUE LAVERNIA is with the Department of Chemical Engineering and Material Science, University of California, Davis and also with the Department of Chemical Engineering and Material Science, University of California, Irvine, Irvine, CA 92697. Contact e-mail: lavernia@uci.edu DIRAN APELIAN is with the Material Processing Institute, Worcester Polytechnic Institute, Worcester, MA 01609.

Manuscript submitted March 28, 2017.

Article published online October 10, 2019

cryogenic temperatures, thereby leading to an increase in the kinetics of grain refinement^[9,10] A high concentration of dislocations is introduced into the microstructure during cryomilling process from the impacts of the powder with the milling media. Within the material, the localization of deformation results in shear bands containing high concentrations of dislocations. In addition to the Frank–Read sources located within the shear bands, the oxide dispersoids themselves may also act as dislocation sources, further increasing the number of dislocations within the material. Rearrangement of the dislocations generated during cryomilling ultimately results in the formation of grain boundaries, as described in references,^[11,12] While a large proportion of dislocations contribute toward the formation of a fine-grained microstructure, some of the dislocations remain within the grain interiors.

The strengthening mechanisms of mechanically alloyed ODS steels have been examined extensively in order to establish the contribution of each strengthening component toward the total strength of a material. It has been shown that dispersion strengthening is the most important contributor to strength,^[13] as randomly distributed nanosized oxide particles are the main obstacles to dislocation motion. The oxides also effectively pin down grain boundaries and thereby inhibit grain growth; the material is also strengthened through a Hall–Petch mechanism. There are many other contributions that can be attributed to the stainless steel matrix,^[14] such as intrinsic lattice resistance to dislocation motion (the Peierl–Nabarro stress), solid solution strengthening of other alloying elements, and dislocation strengthening. ODS steels (Fe-15Cr-1Mo-0.3Ti) with 0.35 wt pct Y₂O₃ can achieve a yield strength as high as 950 MPa after 48 hours of ball milling at room temperature, followed by hot isostatic pressing and hot rolling, to tailor the size of oxide phases and grains.^[15]

A closer look at dispersion strengthening reveals that the most crucial microstructural factor of dislocation–dispersoid interaction is interparticle spacing. Oxide precipitates can be sheared by dislocations when they are small and coherent with the steel matrix.^[16] However, at higher temperatures, the nanoparticles tend to coarsen; moreover, mechanisms are more complex for larger particles when the interface between the oxide and matrix is no longer coherent. When the limiting mechanism is the climb of the dislocation, the critical constraint is proportional to Orowan stress.^[17] When the limiting mechanism in detachment of dislocation, the strengthening effect of dispersoids is going to be inversely proportional to the interparticle spacing. Regardless of how the oxide particles are going to interact with dislocations, the strength of an ODS material increases with decreasing interparticle spacing.

Thus, the strategy for ODS steels is to achieve homogeneous dispersion of nanometric oxides during cryomilling, and prevent the oxide particles from coarsening at high temperature during sintering to activate the oxide dispersion strengthening mechanism.

Homogeneous dispersion can be qualitatively measured by comparing the observed interparticle spacing of the dispersoids with the theoretical value l , given by:

$$l = \sqrt[3]{\frac{4}{3}\pi\left(\frac{d}{2}\right)^3 / f} \quad [1]$$

where d and f are the diameter and volume fraction of the oxide particles, respectively.

Inspection of the published literature reveals that many studies have already been published on the topic of ODS steels,^[18,19] however, our fundamental understanding of the mechanisms that govern the behavior of these systems remains limited. For instance, alloy design, which includes selecting composition and the heat treatment to optimize strength, ductility, and toughness, remains mostly a trial-and-error process. In addition, the variables that control the microstructure and their influence on alloy properties have yet to be investigated in detail. In the current investigation, the primary goals are to study the microstructural evolution of the mixed powders during each step in the processing sequence, to understand the processes that govern the dispersion of the oxide nanoparticles, and to determine the strengthening mechanisms of the cryomilled material.

To accomplish these goals, we first cryomilled two types of oxide particles—yttrium oxide (Y₂O₃) and yttria-stabilized zirconia (YSZ) with the 316L stainless steel separately, which is an alloy with relatively high ductility, strength (40 pct tensile elongation and 450 MPa yield strength in annealed condition),^[20] and good corrosion resistance.^[21] The material also has an interesting phase transformation from face-centered cubic (fcc) to body-centered cubic (bcc) that might be induced either by temperature^[22] and/or strain.^[23] The oxides were chosen since their structural complexity can help restrict diffusional events within the matrix. We then consolidated the material using two different sintering processes: conventional sintering, as well as the Field Assisted Sintering Technique (FAST). The latter allows the system to heat up at a very high rate to limit the grain growth as temperature increases. A bimodal structure (which contains a predetermined fraction of coarse grains),^[24,25] was introduced in some of the sintered samples to toughen the cryomilled material. Advanced microscopy techniques were used to investigate the spatial distribution of oxides, and to identify their relationship with the matrix in order to understand the chemical and diffusional events during mechanical milling and sintering. With reference to mechanical behavior, a careful analysis of strengthening mechanisms is necessary to understand the relative roles of particles dispersion, grain size refinement, as well as the contribution of the matrix at elevated temperatures. In addition, the interactions among dispersoids, dislocations, and grain boundaries were also considered by implementing an existing numerical model.^[26]

II. EXPERIMENTAL

A. Material Selection and Processing

Hoeganaes Corporation (Cinnaminson, NJ) supplied the 316L austenitic stainless steel powder, which was fabricated by water atomization; its chemical composition is given in Table I. The oxide particles used in this study were yttria (Y_2O_3 , Amorphous Material, 99.95 pct, 20-40 nm) and 3 mol pct yttria partially stabilized zirconia (YSZ, Daiichi, 99.95 pct, 75-133 nm). Table II provides the details of the prepared samples—dispersion addition, type of milling media and milling vessel. Weighted powder mixes were measured and V-blended; cryomilling was carried out in a modified Svezgari1S Union Process attritor. Cryomilling with tungsten carbide (WC) media was completed in a modified 01 attritor. The parameters used for cryomilling in liquid nitrogen are shown in Tables III and IV. Test runs showed no evidence of excessive cold welding; thus, no process control agent was used.

The milling media and milling vessel size (Table III) were varied to study the dependence of milling intensity on microstructural evolution of the powders. Eight samples were collected at various milling intervals (0, 0.5, 1, 2, 4, 8, 12 hours) during cryomilling to study the microstructural evolution as a function of milling time.

B. Consolidation and Mechanical Behavior

Two distinct consolidation routes were chosen: conventional sintering and FAST. Comprehensive information about sample IDs composition, and processing routes is listed in Tables V and VI accordingly.

Samples S0-S4_40 pct were conventionally sintered. Sample S1_40 to S3_40 pct were composed of 40 pct cryomilled powders and 60 pct water-atomized 316L powder. 0.75 pct Acrawax lubricant was used for de-molding purposes. The mixed powders were cold pressed at 50 tsi (690 MPa) in rigid dies. The cold pressed specimens were subsequently sintered using Abbott furnace in a 100 pct hydrogen gas atmosphere at 2300°F (1260 °C). Tensile strength was also measured in accordance to ASTM E8. At least 5 specimens of each material were used for mechanical testing. HRA hardness measurements were done using a Wilson Rockwell 504R Hardness Tester. Density was measured using Archimedes' principle per ASTM B962-15.

Sample FAST0-FAST4_40 pct was consolidated *via* FAST. A compressive load of 80 MPa in Φ 19 mm graphite dies at 1273 K (1000 °C) with heating rate of 100 °C/min was used. HRA hardness measurements were obtained using the same methodology described for the conventionally sintered materials. Electric discharge machining (EDM) was used to section 4 mm ×

4 mm × 6 mm specimens from the sintered pillars for compression tests. The loading direction of compression tests was aligned with the loading direction of sintering along the 6 mm height. The compression test was conducted using universal testing machine Intron 8801 at strain rate of $10^{-3} s^{-1}$. Two samples were tested for each material type.

C. Characterization

Nitrogen and oxygen contents of Samples P0-P4 were measured using an inert gas fusion Leco EF-400 nitrogen/oxygen determinator. Laser particle size analysis of the loose powders was performed using a Sympatec Helos BF laser particle size analyzer. Powder morphology of the cryomilled powder was determined from scanning electron microscopy (SEM) micrographs acquired on a FEI XL30 SEM.

For microstructural characterization, the cryomilled powders and sintered materials were mounted in copper-based conductive mounting media, mechanically polished to reveal the cross sections, and studied *via* light microscopy following etching with glyceragia (15 ml HCl + 10 mL Glycerol + 5 mL HNO₃). SEM analysis was conducted on these samples using a FEI Scios dual beam-focused ion beam (FIB)/SEM equipped with Oxford NordlysNano electron backscattered diffraction (EBSD) detectors.

Thin lamellar pieces with an approximate size of 6 μ m × 4 μ m × 50 nm were sectioned from the cross section of loose powder using a FIB for transmission electron microscopy (TEM) and scanning transmission electron microscopy (STEM) analysis using a JEOL 2500 operating at 200 kV. Preparation of the thin lamella was completed with the lowest voltage of 2 kV gallium (Ga) ion beam to minimize a beam damage.

X-ray diffraction (XRD) analysis was performed using Cu-K α radiation ($\lambda = 0.154$ nm) on Scintag XRD. The grain size refinement was quantitated by measuring the full-width at half-maximum (FWHM) of the XRD profile, using Williamson–Hall formula.^[27]

III. RESULTS

A. Characterization of Powder After Cryomilling

SEM images in Figure 1 show the particle morphology, and how it changes as a function of cryomilling time intervals.

They present results of P2 feedstock (316L + 2 wt pct Y_2O_3), and they are representative for all cryomilled powders. The irregular shaped water-atomized SS powders (Figure 1(a)) were flattened into a flake like morphology after the first 1 hour of milling

Table I. Chemical Composition of the Feedstock 316L Stainless Steel

	Cr (Pct)	Ni (Pct)	Mo (Pct)	Si (Pct)	O (Pct)	Mn (Pct)	C (Pct)	P (Pct)	N (Pct)	Fe
316L	16.62	13.90	2.95	0.84	0.39	0.13	0.02	0.02	0.02	bal

All units are given in weight percent.

Table II. Synthesis of the Composite Powders via Cryomilling

Powder ID	Condition	Components	Milling Media	Milling Attritor Diameter (cm)
P0	As-received	316L	–	–
P1	cryomilled	316L	stainless steel	26
P2	cryomilled	316L + 2wt pctY ₂ O ₃	stainless steel	26
P3	cryomilled	316L + 10wt pctYSZ	stainless steel	26
P4	cryomilled	316L + 10 pctwtYSZ	tungsten carbide	8.9

Table III. Processing Parameters Used for Calculations Regarding the Cryomilling Experiments

	P3	P4
Density of Milling Media, ρ_B	8.00 g/cm ³	15.90 g/cm ³
Young's Modulus of Milling media, E []	210 GPa	700 GPa
Diameter of the Milling Media, r_B	6.35 mm	6.35 mm
Ball/Powder Friction Coefficient, μ []	0.15	0.15
Ball to Powder Mass Ratio, C	20:1	20:1
Attritor Diameter, $2R$	0.26 m	0.089 m
Height of the Ball Milling Space	0.32 m	0.14 m
Impeller's Rotational Frequency, F	180 rpm	300 rpm
Total Ball Mass, M	30 kg	1 kg
Milling Time, T	12 h	12 h

Table IV. Physical and Mechanical Properties of 316L at Liquid Nitrogen Temperature (77 K)

Density, ρ_p	Uniaxial Tensile Yield Strength, Y	Shear Work Hardening	
		Factor, K	Index, n
8000 kg/m ³	1670 MPa	1173 MPa	0.132

(Figure 1(b)). Folding and fracturing of powder particles were observed starting from 2 hours of cryomilling (Figure 1(c)). In Figure 1e, after 8 hours, there are barely any flattened particles in view; instead there are uniaxial particles of various sizes, including fine particles less than 5 μm and coarse particles that have not received as much deformation and/or fragmentation. After 12 hours of cryomilling, the particles are more uniform in size, resulting in an average particle size of 15.12 μm (Figure 1(f)).

The powder particle size analysis provides more quantitative results, which shows the measured particles size distributions obey Gaussian distribution. Therefore, the distribution width is cited in the form of the three values: D_{10} , D_{50} , and D_{90} . The D_{50} , the median in the Gaussian distribution, is defined as the diameter of the particles where half of the population lies below this value. As shown in Table VII, the particle size of the powders decreases drastically with reinforcement after cryomilling, especially for P2 and P3, which are milled in the 1S milling vessel using stainless steel media. P4 powder, which was milled in a smaller vessel and attritor using WC media, appears to have a much wider distribution of particle size.

Results of O and N contents are also presented in Table VII. Most of the oxygen originated from the water-atomization process of the feedstock and oxides

that were added during the milling process. Oxidation of the powder particles was effectively prevented in part because the powder was milled in liquid nitrogen.^[28] Nitrogen level increases significantly due to the gas entrapment at the internal surfaces during the folding–unfolding events of the powder particles in the nitrogen.

B. Microstructural Characterization of Powder

Figure 2 shows the X-ray diffraction data obtained from the water-atomized (P0) and cryomilled (P1-P4) powders.

A phase transformation from FCC to BCC was observed after 12 hours of cryomilling for all of the cryomilled powders studied (P1-P4). Also, in Figure 2, peaks from oxide phases, either from Y₂O₃ or YSZ, were not evident in the XRD profiles of P2 or P3. However, peaks from two unique polymorphs of YSZ particles (tetragonal and monoclinic 3YSZ) were revealed in P4, along with peaks diffracted by hexagonal WC. Most likely, the WC particles were fragmented from the WC grinding media during collision events of ball milling and embedded in the stainless steel matrix of the powder particles. The other cryomilled powders (P1-P3) failed to reveal any evidence of WC contamination, because they were milled using grinding media

Table V. Density and Mechanical Properties of the Conventional Sintered Specimens

ID	Mix	Green Density (g/cm ³)	Sintered Density (g/cm ³)	HRA (R/A)	Tensile test				
					0.2 Pctys (MPa)	UTS (MPa)	Elong (Pct)	Impact (Joules)	TRS (MPa)
S0	P0	6.76	7.01	33	231.7	389.6	18.85	81.3	943.9
S1	316L+40 pctP1	6.27	6.63	21	178.6	206.2	2.23	25.8	666.1
S2	316L+40 pctP2	6.15	6.51	23	189.6	228.9	2.26	12.2	600.5
S3	316L+40 pctP3	6.06	6.40	32	194.4	223.4	0.87	6.8	670.9

Table VI. Density, Compressive Strength, and Hardness of the FAST-Sintered Specimens

Sample ID	Mix	Density (g/cm ³)	Compressive Strength (MPa)	Hardness Rockwell A HRA
FAST0	P0	7.762	381.3	53
FAST1	P1	7.763	802.6	66
FAST3	P3	7.161	1462.5	73
FAST3_40 Pct	316L+40 pctP3	7.330	838.4	72
FAST4	P4	7.421	717.2	67
FAST4_40 Pct	316L+40 pctP4	8.080	496.4	59

that was made of the same material as the feedstock stainless steel. Also, the value of FWHM of P4 led to a coarser calculated grain size (51.6 nm, shown in Table VII), when it is compared with that of other cryomilled powders' (< 16 nm).

The X-ray diffraction patterns shown in Figure 3 indicate that the structural change from FCC to BCC actually took place during the first 2 hours of cryomilling.

The first three peaks of FCC structure noted in the 30 and 60 minutes sample disappeared or blended into the background signals after 2 hours of cryomilling. The peaks remained unchanged for longer milling times.

Additional information about microstructure of the cryomilled powders was obtained by FIB of single powder particles. Alternative bands of grains less than 20 nm and elongated grains around 100nm were observed in the cryomilled powder P2, as shown in Figure 4(a) and some parts of Figure 4(b).

The lamella structure suggests that the selected milling time and conditions did not result in the development of an equilibrium microstructure—refined and uniaxial grains. The width of the lamella structure (100 nm in this case) equals to the theoretical minimal interparticle spacing for second phase, if any.^[29] Even though the micrographs shown in the present manuscript were taken on the P2 powder particles, no Y₂O₃ particles were observed in either the STEM or TEM micrograph. This finding supports the theory that Y₂O₃ is not physically incorporated into the powder during the cryomilling process. Any Y₂O₃ would have likely been located at the surface or formerly free surfaces of the cryomilled powder particle, which would not have been observed since material was obtained below any of the surface/former surfaces. In contrast, the YSZ powder were observed under both cryomilled condition (Figure 5(a)) and FAST-sintered condition (Figure 5(b)).

C. Microstructure Characterization of Sintered Sample

The TEM micrographs and electron diffraction patterns of cryomilled powder (P3, 316L+10 wt pct YSZ) and its FAST-sintered specimen (FAST3) are shown in Figure 5 side by side. The original grain size of the water-atomized powder exceeded 1 μm according to the vendor. The grains were refined effectively *via* 12 hours of cryomilling resulting in grain size at around 10 nm as shown in Figure 5(a). After FAST sintering, the average grain size increased up to 91.8 nm, which is still an order of magnitude smaller than that of the feedstock powder. The grain sizes measured from micrographs are in good agreement with the values calculated from XRD profile shown in Figure 2 and in Table VII.

In Figure 6a, the cross-sectional view of the FAST 3 material obtained by SEM shows two different regions separated by prior particle boundaries. The fine-grained regions are more porous and have the lamella structure due to the folding–unfolding process received by the powders during the milling process, whereas the coarse-grained region is free of pores. In Figure 6b, the TEM sample was sectioned *via* FIB at the prior particle boundary presenting the interface of the coarse-grained region and fine-grained region. The YSZ powder, as confirmed by EDS, particle size of which was around 100 nm in the as-received condition, was crushed and fragmented into smaller sizes and stored in the pockets within the fine-grained region. The fine-grained region, in the presence of the YSZ particles, grain size stayed below 100 nm after the FAST-sintering process.

At an even lower magnification, Figure 7 shows a set of cross-sectional optical micrographs of FAST-sintered materials either using water-atomized powder or cryomilled powder.

In Figure 7(a), outline of the prior particle boundaries shows that the water-atomized particles are irregularly shaped. In Figures 7(b) and 7(c), there are two distinct

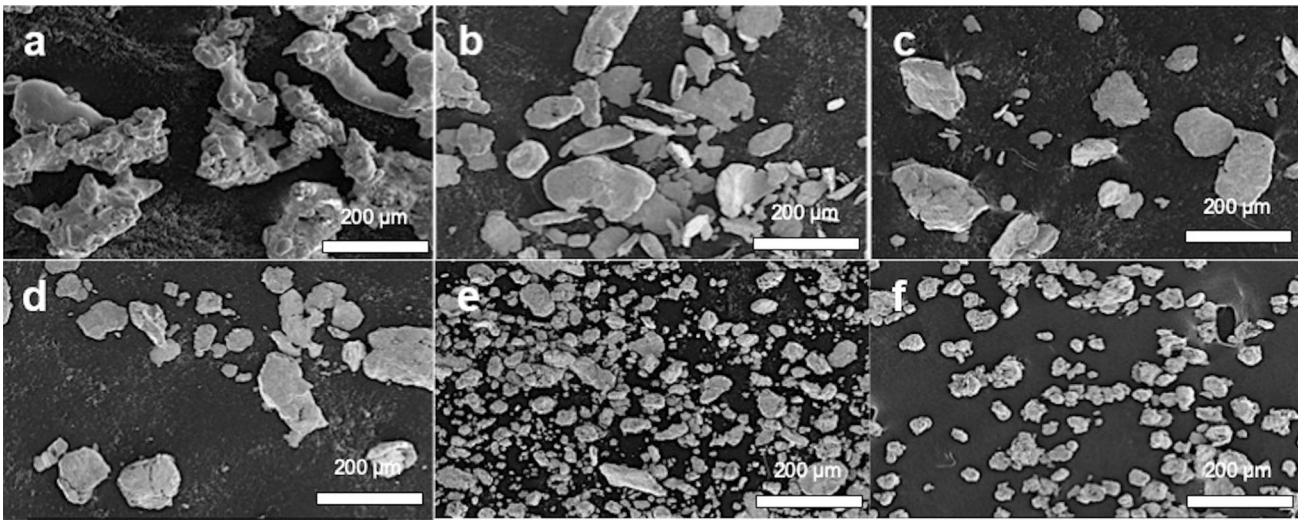


Fig. 1—Secondary electron micrographs showing changes in morphology of the cryomilled powder P2 as a function of milling time: (a) as-atomized, (b) 1 h, (c) 2 h, (d) 4 h, (e) 8 h, and (f) 12 h.

regions: fine-grained regions and coarse-grained regions. The existence of these coarse-grained regions in the material is due the fact that these particles are unequally milled, which in turn is due to the flow irregularities in the milling vessel. This will be discussed in greater depth in the discussion. Figure 7(d) shows the cross section of particles milled in the mini vessel are strips, which indicate flaky powder in 3D. The reinforcement oxide particles, YSZ, are kept in between of the flaky powders.

D. Mechanical Properties

Table V shows the mechanical properties of the conventional sintered specimens made of water-atomized feedstock 316L powder (S0) and mixed powder (S1_40 pct, S2_40 pct, and S3_40 pct) that contain 40 wt pct of cryomilled powder (P1, P2, and P3, respectively). S2_40 pct and S1_40 pct, sintered pieces with and without reinforcement oxide Y_2O_3 , showed similar mechanical properties, including their yield strength and hardness. However, the nanosized oxides were noted to agglomerate and remain at the surfaces or prior particle boundaries of the cryomilled powder P2, diminishing their potency as a reinforcement. Comparing S2_40 pct and S3_40 pct, whose cryomilled powders are reinforced by 2 wt pct Y_2O_3 and 10 wt pct YSZ, respectively, the one with YSZ (S3_40 pct) has higher yield strength as well as hardness; while the one with Y_2O_3 has increased elongation during tensile tests. The difference is mostly attributed to a much higher weight percentage of oxides in the cryomilled powder. Although the oxide particles strengthened the material they also provide sources of defects for crack to nucleate and propagate.

Fracture surface of the tensile specimens are presented in Figure 8.

The wider and deeper dimples revealed in Figure 8(c) provide S0 (sintered as-atomized 316L) with over 20 pct elongation in tensile tests and imply a coarse-grained structure, which is in good agreement with the cross-sectional view of the same sample (Figure 8(a)).

Figure 8(b) shows that oxides were barely located within the grains and rather observed at grain boundaries and particle boundaries for S2_40 pct (sintered as atomized 316L + 40 pct P2). Water-atomized powder with coarser grains and cryomilled powder with finer grains are readily distinguished. Smaller dimples at fracture surface, shown in Figure 8(d), suggest that S2_40 pct fractured in fine-grained regions. Clusters of the nanosized Y_2O_3 particles (confirmed using EDS) were observed at the fracture surface, which might indicate that the origin of the fracture is the agglomerated nanoparticles.

Table VI lists the compressive strength of all the FAST-sintered samples read from stress-strain curves shown in Figure 9.

Compression tests for FAST0, FAST1, and FAST4_40 pct were stopped before fracture because limitation of the test frame, which reached is maximum capabilities. The stress-strain curves show that cryomilling results in significant strengthening, and the sample made of cryomilled 316L(FAST1) doubled the yield strength of regular 316L(FAST0), while maintaining good ductility. The FAST3 material (FAST-sintered P3, 316L + 10 pct YSZ) showed extremely high strength but very limited ductility. Its corresponding bimodal material, which has 40 pct cryomilled powder and 60 pct water-atomized 316L, has relatively high strength and moderate ductility. Similarly, the water-atomized 316L in FAST4_40 pct toughened the material in the same manner as was observed in the bimodal microstructure; ductile coarser grains act as crack blunting object to limit crack propagation through brittle cryomilled regions.

IV. DISCUSSION

A. Strain Energy Model

A mathematical model developed by Lin^[26] was used to calculate and compare the amount of strain energy,

Table VII. Particle Size, O/N Content, and Grain Size of the Powder Samples

	D ₁₀ (μm)	D ₅₀ (μm)	D ₉₀ (μm)	O/N Content (Weight Percent)	Grain Size
P0	27.13	76.12	151.07	0.39/0.02	> 1 μm
P1	35.92	66.65	128.61	–	8.7 nm
P2	5.36	15.12	35.40	0.57/0.13	15.7 nm
P3	8.37	23.31	61.10	–	12.8 nm
P4	13.18	63.48	197.33	–	51.6 nm

Grain size of P0 was measured from optical micrographs, while the grain sizes of P1-P4 were estimated from XRD results using Williamson–Hall relationship.

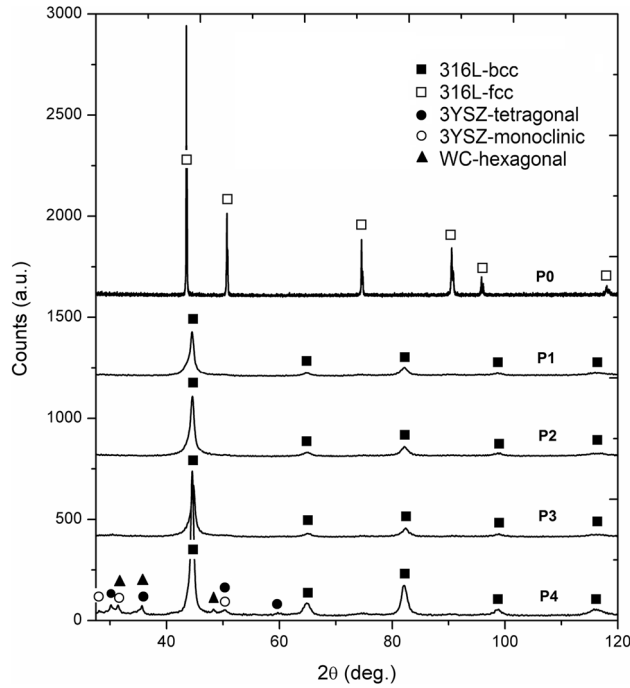


Fig. 2—Phase identification of the XRD patterns of the cryomilled powders P0-P4.

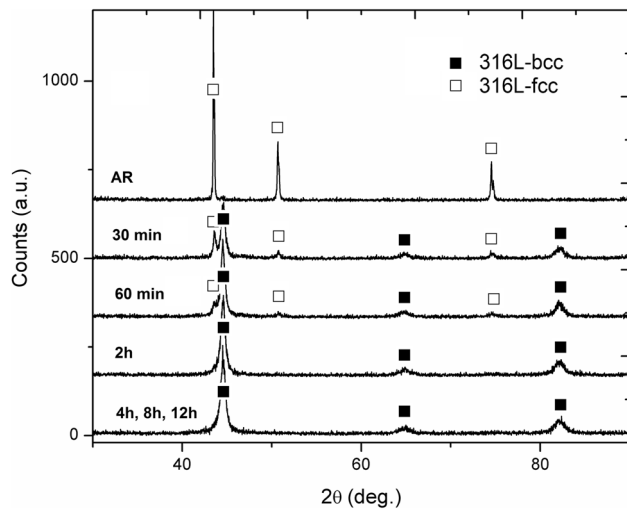


Fig. 3—XRD patterns from powder P2 that was cryomilled for different time intervals, showing the fcc to bcc phase transformation.

U_i , introduced to the powders P3(cryomilled with SS media for 12 hours) and P4 (cryomilled with WC media for 12 hours) during cryomilling. The relationship is defined as follows:

$$U_i = ft(U_{E,\sigma z} + U_{E,\sigma r} + U_S)/m$$

where f is the collision frequency of the given milling process, t is the milling time, and m is the mass of the powder used in the experiment. The model assumes that the entrapped powder during the ball milling process has a cylindrical geometry with a height along z -axis and a radius along r axis in polar coordinates. In the above equation, $U_{E,\sigma z}$ and $U_{E,\sigma r}$ are strain energies introduced by compressive stresses along Z and r , and U_S is the shear strain energy introduced to the entrapped powders from an individual collision. The processing parameters and mechanical properties of 316L at liquid nitrogen temperature used in this calculation are listed in Tables III and IV, respectively.

The results (Table VIII) show that powders milled by the HD01 attritor do not experience as much strain energy (up to two orders of magnitude) as those milled by the 1S attritor configuration, even when a heavier milling media type is used. According to the calculation, the strain energy introduced from single collision per unit mass of powder being milled, $(U_{E,\sigma z} + U_{E,\sigma r} + U_S)/m$, for both systems are similar. However, the biggest difference between the two becomes apparent when the frequency of collisions, f , is considered, since the strain energy introduced to the powder U_i is a product of the strain energy introduced from a single collision multiplied by f and by the milling time t . Since f is mainly determined by the geometry of the vessel (primarily the size, in this case), the absolute number of the milling media, and the rotational speed of the impeller, the HD01 only has ~ 1/80th of the number of collisions compared to the 1S attritor configuration.

B. Grain Refinement in Cryomilled Powder

From a perspective of energetics, creation of grain boundaries requires a certain level of energy input from milling events. Higher strain energy introduced to the system potentially leads to finer grain structure. Since the cryomilling setup that utilizes a smaller milling container and attritor imparts less strain energy (refer to Table VIII) to the powder, P4 powder remained flat-tened and results in much larger powder particle size

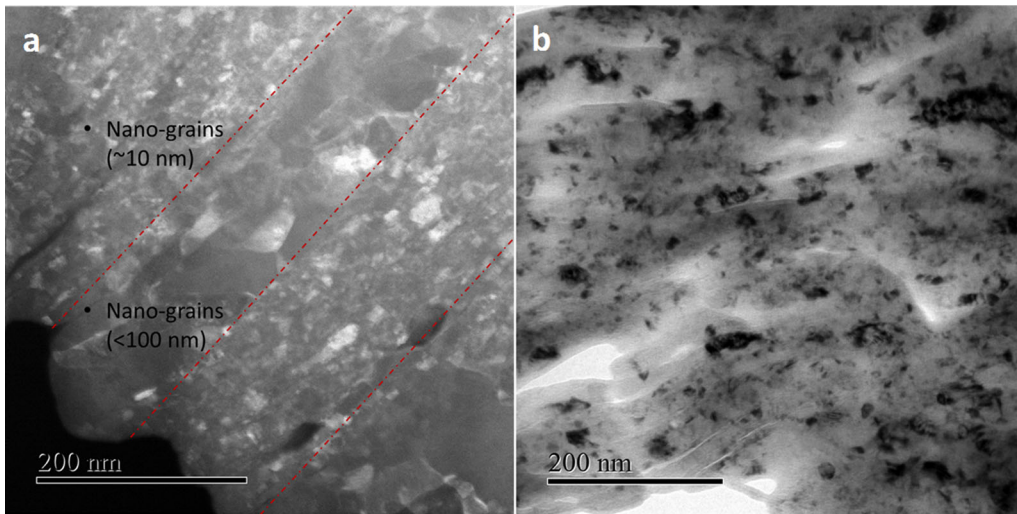


Fig. 4—STEM (a) and TEM (b) micrographs of cryomilled powder P2.

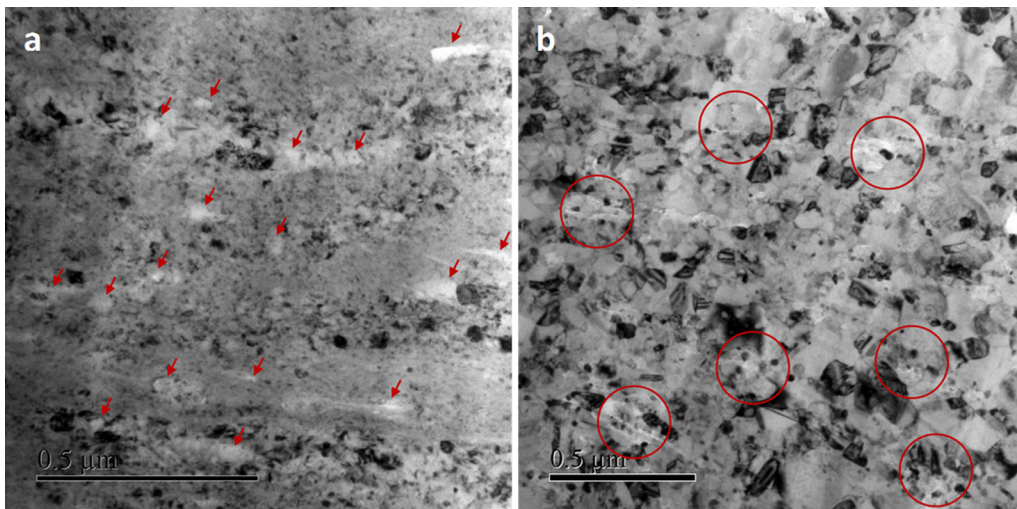


Fig. 5—TEM micrographs of (a) cryomilled powder sample P3 and (b) sintered FAST3. YSZ particles are identified using red arrows and circles in (a) and (b), respectively (Color figure online).

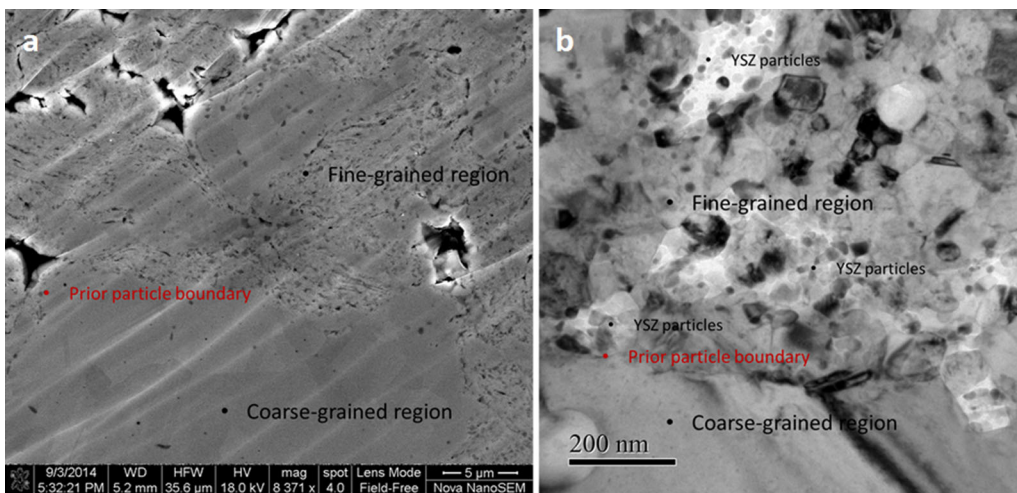


Fig. 6—(a) SEM and (b) TEM micrographs of FAST3 (FAST-sintered P3).

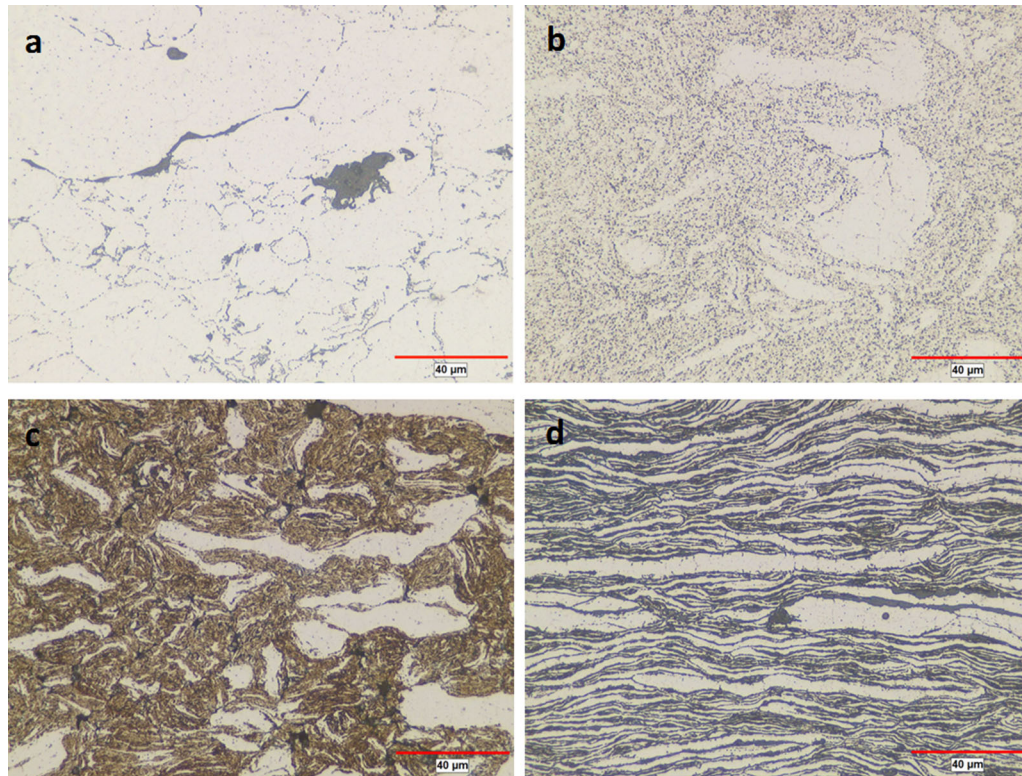


Fig. 7—Cross sections of the FAST-sintered samples composed of (a) water-atomized 316L powder P0, (b) cryomilled P2, (c) cryomilled P3, and (d) cryomilled P4.

compared to other cryomilled powders, as shown in Figure 7(d).

For a given milling experimental arrangement, the average grain size decreases with milling time until it reaches a minimum value, which is a characteristic for different metals.^[30] The magnitude of this minimum grain size has been argued to depend on various factors, including melting point of the metal/alloy, active energy for diffusion, and normalized hardness of the material.^[9] During mechanical milling, two competing microstructural processes occur which ultimately determine the final grain size of the milled metal: grain refinement and grain recovery. The former one is generated by dislocations of nucleation and multiplication, and it hardens the material; the latter happens through recombination and annihilation of dislocations, and it softens the material. The knowledge infers that a relationship between the minimum grain size (d_{\min}) and the critical equilibrium distance of two edge dislocations (l_c) exists when the material is under the maximum applied stress, and thus the dislocation density is saturated. Data fitting of Fe, Cr, and Ni^[31] leads to a following empirical relationship: $d_{\min} = l_c^{1.3}$, where $l_c = \frac{3Gb}{\pi(1-\nu)H}$ is determined when the repulsive force between two dislocations is cancelled out by the applied stress. Using the data presented in Table IX, the minimal grain size for 316L could be in the range of $d_{\min} = 19.69\text{--}43.65\text{nm}$. It is important to note that the model considers equilibrium values; in practice, this is an overestimation of the average grain size because l_c can be overcome by

additional stress, although it is not a stable configuration during cryomilling.

The estimated grain size of the 12 hours cryomilled powder using XRD analysis yields a range of the same magnitude: 8.7–15.7 nm. X-rays penetrate a considerable depth of the sample, and therefore capture the entire substructures, including dislocation walls or subgrain boundaries, so the calculated values usually appear to be lower than actual grain size. Also, since the Williamson–Hall estimation is based on Scherrer’s formula, it is best for nearly spherical grains, whereas for the severely deformed grains developed during cryomilling is not the case.

The size of the cryomilled grains observed in TEM (Figures 4(a), 4(b) and 5(a)) is in the same order of magnitude with the theoretical minimum grain size and grain size estimated from XRD. Also, as shown in Figure 4(a), alternating bands containing two different grain sizes were observed in the cryomilled particles. It appears to be that the nanograin region (where $d < 20$ nm) achieved the theoretical minimum grain size, while the other bands (where $d \sim 100$ nm) are still in process of refinement.

The ability to comprehensively represent the microstructure of the cryomilled material through TEM/STEM micrographs presented in the investigation is limited, since all the observations were made on the thin FIB prepared lamella. A low magnification view provided by optical micrographs reveals a much broader field of view. A bimodal structure (shown in

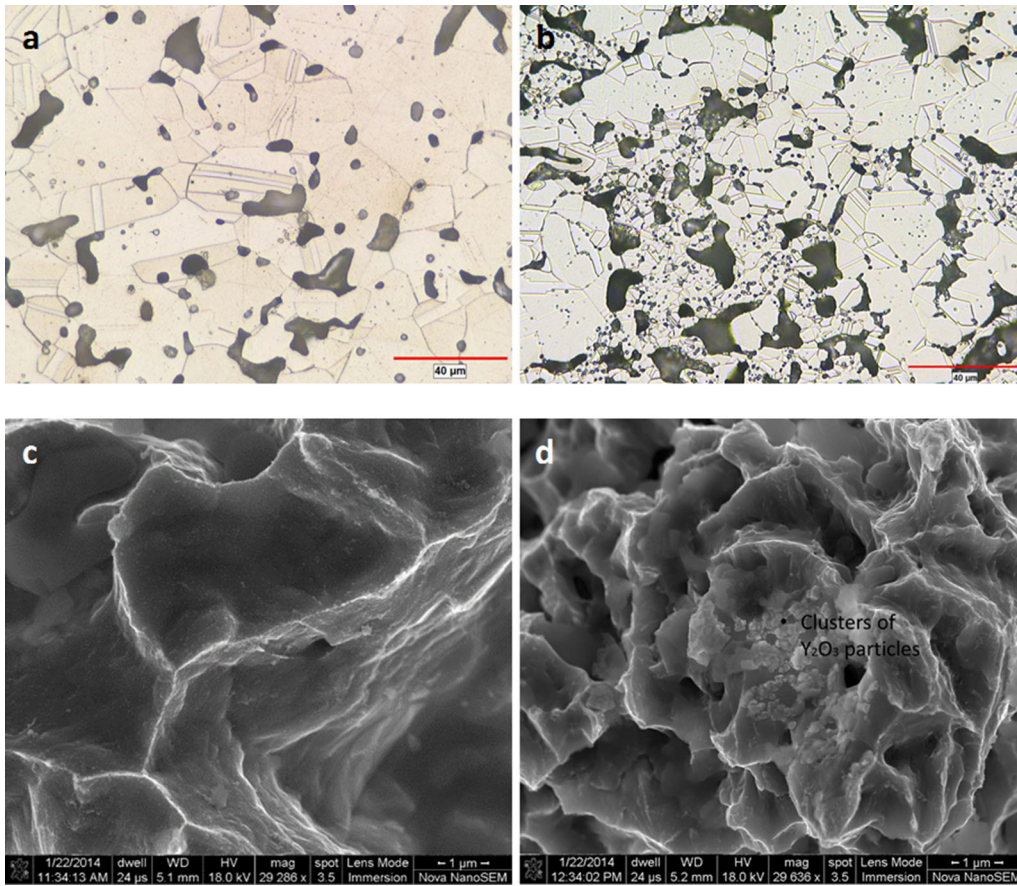


Fig. 8—Cross sections and fracture surface of conventional sintered tensile bars: (a) and (c) are for S0 (water atomized 316L), and (b) and (d) are for S2_40 pct (water atomized 316L with 40 pct cryomilled 316L).

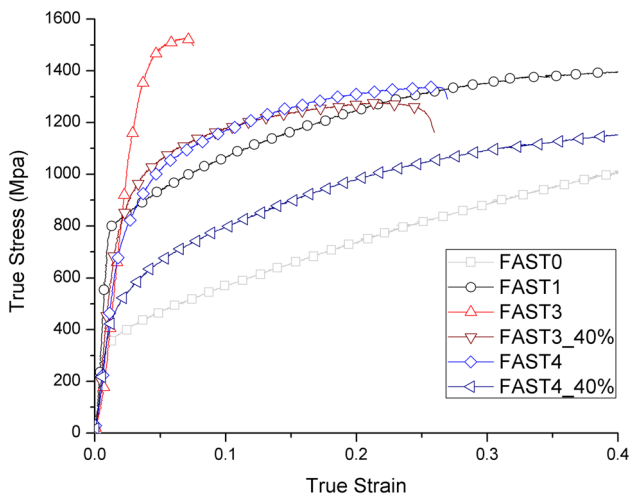


Fig. 9—Compressive stress–strain curves for all FAST-sintered specimens.

Figures 7(b) and 7(c) for FAST2 (sintered P2, 316L with 2 wt pct Y_2O_3) and FAST3 (sintered P3, 316L with 10 wt pct YSZ) evolved not through the sintering process, rather than addition of coarser grained material. In both cases, a fraction of lighter and coarser particles were shown in the micrograph. The lighter regions have much

larger grain size and twin boundaries, whereas the darker regions consist of fine grains and oxides. The origin of the uneven milling arises from the configuration of the 1s mill, which has some “dead” spots where particles do not experience much mechanical milling. The powders that trapped at these dead spots barely experienced any deformation and retained their original microstructure.

In summary, with experimental conditions used herein (1S, 180 rpm, SS media) and 12 hours milling time, the 316L powder particle reaches its final stage of grain refinement; a fraction of the grains exhibit the theoretical grain size of the material. Further refinement of the structure could possibly be achieved by extending the milling time, or by manipulating processing parameters, such as the ball to powder ratio, ball mill configuration, number, and size of the milling media, *etc.*

C. Dispersion of Oxides

During mechanical alloying, a mixture of stainless steel base powders and oxide particles for reinforcement is milled for a long period of time in an attrition ball mill. The severe plastic deformation caused by the collisions between balls or between balls and the wall of stainless steel vessel facilitates both grain refinement of base powder and dispersion of oxides. A three-stage

Table VIII. Processing Parameters Used for Strain Energy Calculation

		Unit	P3 (SS, 1s)	P4 (WC, HD01)
Frequency of Collisions	f	s ⁻¹	252581.9	3117.9
Time of Milling	t	s	12 × 60 × 60	12 × 60 × 60
U introduced by Normal Strain/Stress Along z	$U_{E, \sigma z}$	J	183.9×10^{-5}	12.7×10^{-5}
U introduced by Normal Strain/Stress Along r	$U_{E, \sigma r}$	J	71.9×10^{-5}	0.343×10^{-5}
U introduced by Shear Strain/Stress	U_s	J	25.4×10^{-5}	5.665×10^{-5}
Mass of Powder	m	kg	1.5	0.1
Strain Energy Introduced to the Powder	U_i	J/kg	2.05×10^7	2.52×10^5

Table IX. Parameters of 316L Used in Minimum Grain Size Calculation

	Shear Modulus, G	Burgers Vector, b	Poisson's Ratio, ν	Hardness, H
316L	74–82 GPa	248.2 pm	0.265–0.275	1700–2200 MPa

formation mechanism of oxide nanoparticles proposed by Hsiung's group^[32] is believed to be the most effective way to form stable oxides in a ferritic matrix during ball milling. The first stage is fragmentation of starting oxide particles to form dispersed nanometric fragments. The second stage is amorphization of the fragments in the matrix material. In the third stage, the amorphous oxide clusters grow into oxide nanoparticles with a stoichiometric complex-oxide core and a solute-enriched shell during subsequent consolidation. In the current study, the stainless steel powder was milled in liquid nitrogen at 77 K (− 196 °C) to limit recovery, minimize oxidation, and increase the kinetics of the nanostructure formation. The question at hand is whether the powder particles of interest obey the same behavior in cryogenic conditions during ball milling as they do under “room temperature” conditions, and to what extent?

The microstructure of S2_40 pct, which has 40 pct P2 powder (cryomilled 316L + 2 wt pct Y₂O₃), suggests that low temperatures milling might deactivate the amorphization processes proposed in Hsiung *et al.*'s three-stage formation mechanism. In the center of the dimple blossom (Figure 8(d)), a cluster of Y₂O₃ particles was determined by EDX. Note that size and shape of the Y₂O₃ particles retained the same as their as-received condition. The granular faceted morphology suggests that these particles have not experienced fracture or amorphization as one might expect from room-temperature ball milling.

Interestingly, under the same milling and sintering conditions, YSZ powders in S3 show evidence of fragmentation and re-agglomeration. In Figure 5(b), pockets in the matrix that contain a cluster of small YSZ crystallites were observed. Compared to their as-received condition, YSZ particles detected in these pockets have a much smaller particle size, which implies the 104 nm YSZ particles are crushed into 20 nm (or smaller) fragments during cryomilling. The near-spherical shape of the crushed YSZ particles suggests that the corners of the fragments were rounded either *via* amorphization during milling or surface diffusional events during

sintering. Also, the average interparticle spacing between the pockets is approximately in the same range as 172 nm, which is the theoretical interparticle spacing of the added 10 wt pct YSZ at its given size using Eq. [1]. This observation implies that the particles have been evenly distributed in the matrix but they fragmented during milling. The same microstructure also reveals the poorly structured interface between the nano-oxides clusters and the matrix. The voids were probably developed due to volume change of the YSZ during sintering, which is either caused by the large difference in thermal expansion coefficients of YSZ and 316L or the phase transformation of YSZ as temperature changes or both. However, the porous oxide clusters in the pockets cannot bear as much load as their fully dense counterparts, and the weakly bonded interface between the clusters and the steel matrix might provide an easier pathway for crack propagation. Tougher particles are thus preferred in order to retain their strengthening effect in the final product. In short, cryomilling of 316L with 10 wt pct YSZ proceeded to the second stage suggested by Hsiung, yet the system did not reach the third stage, in which the material forms coherent diffusional structure between the oxides and the iron-based matrix.

There are a number of factors that are responsible for the enhanced dispersion of YSZ in the 316L matrix in comparison to Y₂O₃. First, the density of YSZ particles (6.05 g/cm³) is higher, and closer to that of the stainless steel powder. By comparison, the density of the Y₂O₃ particles is 5.01 g/cm³. This similarity in density allowed the YSZ particles stay at the bottom of the milling vessel, which results in better mixing with 316L powder during milling. Second, YSZ particles were added in a much higher weight percent (10 wt pct) as compared to the Y₂O₃ particles (2 wt pct). This difference in weight percentage creates more opportunities for the YSZ particles to be involved with collisions and shearing events during mechanical milling. Moreover, TEM micrographs of as-received oxides and information from the vendors point out that both types of oxides readily

agglomerate. Agglomeration is a common problem for nanometric powders, which tend to group together in order to diminish their high surface energy. Although both oxide powders agglomerate, the secondary bonding of the YSZ powder is not as strong and fractures during milling.

In light of the preceding discussion, if no fragmentation–amorphization–precipitation (the three-stage mechanism by Hsiung^[32]) is expected and the secondary bonding of nano-oxides can be interrupted during cryomilling, dispersion of the oxide phase then solely relies on the development of internal surface area. When particles are flattened or bent during milling, surface of the particle increases and new surfaces are formed. The more surface area, the better dispersion of oxides; less surface area limits the possible locations of oxide particles causing severe agglomeration issues. When fresh metal surfaces press on other fresh metal surfaces during milling, cold welding takes place resulting in metallurgical bonded agglomerate. Depending on the relative orientations of the particles, the interface can transform to part of grain interior or become grain boundary. Therefore, if oxide particles are attached to the fresh surfaces, they will appear inside a grain or, most frequently in this case, at the grain boundary after cold welding. The results of this process could be proved by Figure 8(b), where oxides located at grain boundaries were observed. However, if the cold welding does not occur, the contacting surfaces of two particles will become a prior particle boundary or sometimes voids on the scale of micron. As shown in Figure 7, most of the oxides are trapped in between the flattened particles.

Since the three-stage mechanism of oxide dispersion proposed by Hsiung for room-temperature ball milling does not occur during cryomilling of 316L. The final spatial location of the nano-oxides is determined by the development of the internal surfaces during cryomilling, which can be controlled by altering some of the milling parameters including milling time, milling intensity, and milling media. Bonding between nanometric particles in as-received condition plays an important role in the further separation and dispersion of the oxide powder particles. Technical challenges related to dispersion of oxides can possibly be overcome by creating hierarchical materials. This was achieved here by mixing atomized coarse-grained particles with cryomilled particles during sintering. In the present investigation, the hierarchy of the spacing of the constitutive phase led to tougher structures after sintering.

D. Mechanical Behavior of Cryomilled Material

The mechanical properties of the cryomilled materials belie the complexity of their mechanical behavior. In this following subsection, efforts have been made to determine the mechanisms that govern the mechanical behavior of the sintered specimen made from cryomilled powder.

The study focuses on FAST3 (made of P3, cryomilled 316L + 10 wt pct YSZ), of which achieved good dispersion of the oxide particles and retention of nanoscale average grain sizes after FAST sintering (Figures 5 and

6). However, since its microstructure is also characterized by pores, a high concentration of oxide particles, fragments of these particles, and the poorly structured interface between oxide particles and matrix, more in-depth analysis is required in order to understand whether the material obeys strengthening mechanisms of ODS alloys or composite materials. Mathematical models based on oxide dispersion strengthening and load transferring, respectively, are used to analyze the yield strength of FAST-sintered specimens.

Estimation of yield strengths (σ_y) of interest were given using the following equation:

$$\sigma_y = 3.06 \times H_V \quad [2]$$

where H_V is Vickers hardness and 3.06 is a material-dependent factor determined by Busby *et al.*^[33] for steels. Hardness values and yield strengths are given in Table VI, along with the compressive strengths for comparison. Results of FAST0 and FAST1 were used as control groups of unmilled material and cryomilled material without reinforcement, respectively.

1. Oxide dispersion strengthening

In ODS alloys, the strength (σ_y) can be mostly attributed to three different components: Orowan strengthening component (σ_{Orowan}), Hall–Petch strengthening component (σ_{HP}), and the matrix strength component (σ_M).

$$\sigma_y = \sigma_{\text{Orowan}} + \sigma_{\text{HP}} + \sigma_M \quad [3]$$

Contribution of Orowan strengthening can be calculated using the following equation^[13]:

$$\sigma_{\text{orowan}} = \alpha \mu b \sqrt{Nd} \quad [4]$$

where α is a constant and equals to 1.0 for impenetrable particles. μ is the shear modulus of the metal matrix, which equals to 82 Gpa for 316L. b is Burgers vector of iron, which gives 0.286 nm. N is the number density of the particle, and bears a relationship with interparticle spacing: $N = \frac{1}{l^3}$, and $l = 172.27$ nm in this case. d is the average diameter of the dispersed particles, $d = 104$ nm. All these numbers yield the Orowan strengthening component for 10 wt pct YSZ (12.9 vol pct) reinforced 316L matrix $\sigma_{\text{orowan}} = 105.6$ MPa.

At the same time, in Table X, the difference of measured yield strengths of cryomilled material with and without oxide reinforcement can easily be calculated: $\sigma_y(\text{FAST3}) - \sigma_y(\text{FAST1}) = 374.2$ MPa. The fact that this value is over three times higher than σ_{orowan} is attributable to differences in grain sizes.

When estimation of Hall–Petch strengthening is presented, D_0 , D_1 , and D_3 are used for the average grain sizes of FAST0, FAST1, and FAST3, respectively. Hall–Petch strengthening component has an inverse relationship with the square root of grain size D :

$$\sigma_{\text{HP}} = \frac{K}{\sqrt{D}} = \frac{535 \text{ MPa}}{\sqrt{D}} \quad [5]$$

Table X. Calculated Grain Sizes and Observed Grain Sizes of FAST-Sintered Specimens

Sample ID	Compressive Strength (MPa)	Hardness (HV)	σ_y (MPa)	σ_{Orowan} (MPa)	σ_{HP} (MPa)	σ_M (MPa)	D_{Calc} (um)	D_{Observed} (um)
FAST0	381.3	176.13	538.96	–	$535/\sqrt{D_0}$	290	4	~ 5
FAST1	802.6	313.98	960.78	–	$535/\sqrt{D_1}$	290	1	~ 1
FAST3	1462.5	436.26	1334.96	105	$535/\sqrt{D_3}$	290	0.5	0.1

Table XI. Measured Strength and Density of the Two FAST-Sintered Composite Samples

Sample ID	Mix 1 (60 Pct)					Mix 2 (40 Pct)					
	σ_c (MPa)	ρ (g/cm ³)	ID	σ_c (MPa)	ρ (g/cm ³)	ID	σ_c (MPa)	ρ (g/cm ³)	$\sigma_{c,\text{lower}}$ (MPa)	$\sigma_{c,\text{upper}}$ (MPa)	ρ_{calc} (g/cm ³)
FAST3_40 Pct	838.4	7.330	FAST0	381.3	7.762	FAST3	1462.5	7.161	443.2	813.4	7.52
FAST4_40 Pct	496.4	8.080				FAST4	717.2	7.421	443.2	511.4	7.63

535 MPa-m^{1/2} is taken for K as estimation according to Lee.^[13]

In presence of an oxide phase, small particles act to prevent the motion of grain boundaries by exerting a pinning pressure. Thus, although the average grain sizes of the cryomilled powders P1 and P3 are similar to each other, their grain sizes deviate from each other after sintering. However, previous discussion also points out the unintentional bimodal distributions of grains of these two materials (Figure 7(b) for FAST1 and 7c for FAST3). The large difference in the two modes of the distribution therefore poses difficulties in terms of providing representative grain sizes for Hall–Petch relationship. Therefore, a theoretical approach is taken to verify the possibility of the oxide strengthening mechanism being the dominant mechanism of the cryomilled material's mechanical behavior.

In Table X, contributions of different strengthening components are listed in the cropped region for all three materials. The σ_M is obtained from a very large grain 316L.^[34] Since all other terms (σ_y , σ_{Orowan} , and σ_M) which contribute toward the overall strength of the material are determined either through calculations or through references, σ_{HP} is the only unknown. The D_0 , D_1 , and D_3 obtained from this calculation can then be directly compared to the observed grain sizes. The results shown in the last two columns in Table X (D_{Calc} and D_{Observed}) shows a good match with each other, suggesting that oxide dispersion strengthening could be the dominant strengthening mechanism in cryomilled ODS steels. Compared to D_{Observed} , slightly larger values of D_{Calc} of the cryomilled powder are prompted by the coarse grains of the unintentionally bimodal structure. Before any conclusion can be drawn, the examination of the other possibility is necessary.

2. Load transfer

When high volume fraction of oxide phase is added to the metal matrix, it could also form a discontinuously reinforced composite material. In this case, the exact

strength of the material is difficult to be generalized by a single equation; instead it is helpful to consider an upper bound and a lower bound of the strength.^[35,36]

The upper bound of strength (σ_u) can be estimated by the well-known rule of mixtures. As the load on a composite is increased, load is redistributed between matrix and the oxide phase until general yield or fracture of one of them occurs.

$$\sigma_u = f_v \sigma_{\text{YSZ}} + (1 - f_v) \sigma_{316L}$$

The lower strength value (σ_l) is given in the below equation, which can be thought of as the worst-case scenario. In this case, a continuous, ductile matrix containing strong reinforcing particles; the lower limit for the composite strength is then the yield strength of the matrix enhanced slightly by the plastic constraint imposed by the reinforcement.

$$\sigma_l = \sigma_{316L} \left(1 + \frac{1}{16} \frac{f_V^{1/2}}{1 - f_V^{1/2}} \right)$$

To calculate the above two strength values, σ_{316L} is taken from the yield strength of FAST1 (cryomilled material without oxide reinforcement): $\sigma_{316L} = 960.78$ Mpa. Recall that $f_v = 12.7$ pct for the YSZ reinforced material. The calculation (Table XI) gives $\sigma_u = 1225.1$ Mpa and $\sigma_l = 994.4$ Mpa of FAST3, whose upper bound is still lower than the yield strength of the measured value (1335.0 MPa). Moreover, the bulk strength of YSZ was used in this calculation: $\sigma_{\text{YSZ}} = 3000$ Mpa, whereas YSZ are clustered nanoparticles in reality, which lead to an even lower calculated upper bound value. Thus, the approximation of strength using particle reinforced composite material model does not capture how the material has been strengthened completely; the model based on oxide dispersion strengthening appears to more accurately describe the case for cryomilled ODS steels.

E. Mechanical Behavior of the Bimodal Material

In addition to the sintered materials that are fabricated of only cryomilled powders, a bimodal material consisting of 60 pct as-atomized and 40 pct cryomilled powders was fabricated. The cryomilled powder, with an ultrahigh strength, was blended with ductile large grain as-atomized powder to increase the strength while retaining the ductility of the material.^[8,24] Using the concept of load-transfer mechanism, the theoretical lower bound ($\sigma_{c,lower}$) and upper bound ($\sigma_{c,upper}$) of the compressive strengths can be calculated for FAST3_40 pct and FAST4_40 pct. Both samples have 60 pct water-atomized 316L and 40 pct cryomilled powder reinforced by YSZ. The difference is that the cryomilled powders P3 and P4 were milled in different conditions (size of milling vessel and milling media) that led to two different morphologies of cryomilled powder (Figure 7).

The results in Table XI show that the compressive strength of FAST3_40 pct is 838.4 MPa, and its calculated lower and upper bounds give a range of 443.2–813.4 MPa; while the compressive strength of FAST4_40 pct is 496.4 MPa and its calculated range is 443.2–511.4 MPa. In both cases, the measured strength is closer to the upper bound and within the reasonable error (+ 2.4 and – 3.0 pct). This indicates the strength of the mixed powders at the given ratio follows the rule of mixtures, which represents optimal strengthening of the composite material.

Composite materials, using the same as-atomized powders and cryomilled powder were fabricated *via* conventional sintering. All of the properties measured for composite materials that contain cryomilled powders have lower values than their counterparts of the regular 316L sample (S0), which suggests that the presence of internal flaws in the cryomilled powder, primarily pores, is detrimental to the mechanical behavior of the composite material. The presence of pores was attributed to the absence of a superimposed during conventional sintering and hence the cryomilled particles are unlikely to deform due to their high strength. Also, as seen in Figure 8, the water-atomized 316L particles were separated, and therefore did not contribute to the ductility. The observed properties of composite materials can be enhanced if an optimal fraction of cryomilled powder can be found that provide dispersion strengthening without affecting the sintering behavior of the regular 316L powders.

V. CONCLUSIONS

ODS steels have been developed as a promising structural material at high temperature. In the present study, nanometric oxides were incorporated into a cryogenic ball milling to fabricate the ODS steels with 316L as the matrix. From the results, we are able to draw the below-mentioned conclusions.

- Minimum grain size of 316 L can be achieved *via* 12 hours of cryomilling in 1s milling vessel-using 316L as milling media. However, alternative bands of

minimum size grains (~ 10 nm) and coarser grains (~ 100 nm) were observed in the cryomilled powder. The cross section of the sintered specimen reveals that there is a fraction of large grain particles (~5 μm), which have not experienced as much fracturing and deformation as the others due to the configuration of the milling setup. FAST-sintering technique is able to retain the grain size at 100 nm in presence of the dispersed oxide particles.

- Lower strain energy introduced to system results in flaky shaped powder particles of P4. The flaky morphology and relatively large grains suggest that the powder particles were flattened *via* collisions between the milling media and wall of milling vessel, but not yet starting to refining the grains or achieving the homogeneous structure. More strain energy introduced by milling requires longer milling time, higher rotational speed of impeller, more milling media to increase the possibility of collision events, *etc.*
- A three-step mechanism for dispersion nanometric oxides was identified in literature for room-temperature conventional ball milling. However, no evidence for such mechanism was shown in the cryomilled powder. The oxides added to cryomilling in the given system were dispersed through the development of internal surface area, and largely depend on their own properties. As a result, Y_2O_3 particles that have agglomeration issue in as-received condition stay agglomerated and get coarsened after milling, whereas YSZ particles were successfully distributed throughout the matrix, having its inter-particle spacing equals to the theoretical value. The YSZ particles were crushed into smaller pieces during milling due to the low toughness.
- FAST-sintered cryomilled material has extremely high strength due to the fine grain size, high volume fraction of oxides, and relatively denser body. The strength of the cryomilled material with its reinforcement oxides well dispersed in the matrix was estimated by deconvoluting the strengthening mechanisms into Orowan strengthening, Hall–Petch strengthening, and solid solution strengthening.
- Bimodal structures of cryomilled powder and regular 316L powder were able to provide a combination of high strength and good ductility. The strength of the composite material obeys rule of mixture. The microstructure of the conventional sintered specimens reveals the high volume of porosities, which become the weak points of the material and have a detrimental effect on the mechanical behavior.

ACKNOWLEDGMENTS

This research project was supported by the Hoeganaes Corporation and the Materials Design Institute, funded by the LANL/UC Davis Education Research Collaboration, Los Alamos National Laboratory (LANS Subcontract No. 75 782-001-09).

REFERENCES

1. C.C. Chan: *Proc. IEEE*, 2007, vol. 95, pp. 704–18.
2. M.S. El-Genk and J.-M. Tournier: *J. Nucl. Mater.*, 2005, vol. 340, pp. 93–112.
3. S. Ukai, S. Ohtsuka, T. Kaito, H. Sakasegawa, N. Chikata, S. Hayashi, and S. Ohnuki: *Mater. Sci. Eng. A*, 2009, vols. 510–511, pp. 115–20.
4. T. Okuda and M. Fujiwara: *J. Mater. Sci. Lett.*, 1995, vol. 14, pp. 1600–03.
5. C. Hin and B.D. Wirth: *J. Nucl. Mater.*, 2010, vol. 402, pp. 30–37.
6. J.R. Rieken, I.E. Anderson, M.J. Kramer, G.R. Odette, E. Stergar, and E. Haney: *J. Nucl. Mater.*, 2012, vol. 428, pp. 65–75.
7. Y. Chen, K. Sridharan, T.R. Allen, and S. Ukai: *J. Nucl. Mater.*, 2006, vol. 359, pp. 50–58.
8. E.J. Lavernia, B.Q. Han, and J.M. Schoenung: *Mater. Sci. Eng. A*, 2008, vol. 493, pp. 207–14.
9. F.A. Mohamed: *Mater. Sci. Eng. A*, 2010, vol. 527, pp. 2157–2162.
10. D.B. Witkin and E.J. Lavernia: *Prog. Mater. Sci.*, 2006, vol. 51, pp. 1–60.
11. F.A. Mohamed and Y. Xun: *Mater. Sci. Eng. A*, 2003, vol. 354, pp. 133–39.
12. N. Yang, J.K. Yee, Z. Zhang, L. Kurmanaeva, P. Cappillino, V. Stavila, E.J. Lavernia, and C. San Marchi: *Acta Mater.*, 2015, vol. 82, pp. 41–50.
13. J.H. Lee: *Appl. Mech. Mater.*, 2011, vol. 87, pp. 243–48.
14. Z. Zhang and D. Chen: *Scr. Mater.*, 2006, vol. 54 (7), pp. 1321–26.
15. S. Noh, B. Choi, S. Kang, and T. Kim: *Nucl. Eng. Technol.*, 2014, vol. 46, pp. 857–62.
16. K. Lu, L. Lu, and S. Suresh: *Science*, 2009, vol. 324, pp. 349–52.
17. E. Arzt: *Acta Mater.*, 1998, vol. 46, pp. 5611–26.
18. R.L. Klueh, P.J. Maziasz, I.S. Kim, L. Heatherly, D.T. Hoelzer, N. Hashimoto, E.A. Kenik, and K. Miyahara: *J. Nucl. Mater.*, 2002, vols. 307–311, pp. 773–77.
19. R.L. Klueh, J.P. Shingledecker, R.W. Swindeman, and D.T. Hoelzer: *J. Nucl. Mater.*, 2005, vol. 341, pp. 103–14.
20. R.K. Desu, H. Nitin Krishnamurthy, A. Balu, A.K. Gupta, and S.K. Singh: *J. Mater. Res. Technol.*, 2015, vol. 5, pp. 1–8.
21. Y. Hedberg, M. Norell, P. Linhardt, H. Bergqvist, and I. Odnevall Wallinder: *Int. J. Electrochem. Sci.*, 2012, vol. 7, pp. 11655–77.
22. S.W. Nam: *Mater. Sci. Eng. A*, 2002, vol. 322, pp. 64–72.
23. C. Garion, B. Skoczeń, and S. Sgobba: *Int. J. Plast.*, 2006, vol. 22, pp. 1234–64.
24. B.O. Han, E.J. Lavernia, Z. Lee, S. Nutt, and D. Witkin: *Metall. Mater. Trans. A*, 2005, vol. 36A, pp. 957–65.
25. H. Yang, E.J. Lavernia, and J.M. Schoenung: *Philos. Mag. Lett.*, 2015, vol. 95, pp. 177–86.
26. Y. Lin, B. Yao, Z. Zhang, Y. Li, Y. Sohn, J.M. Schoenung, and E.J. Lavernia: *Metall. Mater. Trans. A*, 2012, vol. 43A, pp. 4247–57.
27. T. Ungár and A. Borbély: *Appl. Phys. Lett.*, 1996, vol. 69, pp. 3173–75.
28. C. Goujon, P. Goeuriot, P. Delcroix, and G. Le Caër: *J. Alloys Compd.*, 2001, vol. 315, pp. 276–83.
29. C. Suryanarayana: *Prog. Mater. Sci.*, 2001, vol. 46, pp. 1–184.
30. H.-J. Fecht: *Nanostruct. Mater.*, 1995, vol. 6, pp. 33–42.
31. F.A. Mohamed: *Acta Mater.*, 2003, vol. 51, pp. 4107–19.
32. L. Hsiung, M. Fluss, S. Tumey, J. Kuntz, B. El-Dasher, M. Wall, B. Choi, A. Kimura, F. Willaime, and Y. Serruys: *J. Nucl. Mater.*, 2011, vol. 409, pp. 72–79.
33. J.T. Busby, M.C. Hash, and G.S. Was: *J. Nucl. Mater.*, 2005, vol. 336, pp. 267–78.
34. AKSteel: *Stainless Steel 316/316L Product Data Bulletin*, 2013, pp. 2–4.
35. S. Ahmed and F.R. Jones: *J. Mater. Sci.*, 1990, vol. 25, pp. 4933–42.
36. B. Avitzur: *J. Eng. Ind.*, 1973, vol. 95, pp. 827–34.

Publisher's Note Springer Nature remains neutral with regard to jurisdictional claims in published maps and institutional affiliations.